IDENTIFYING BACKBONES IN THREE-DIMENSIONAL DISCRETE FRACTURE NETWORKS: A BIPARTITE GRAPH-BASED APPROACH[*]

JEFFREY D. HYMAN[†], ARIC HAGBERG[‡], DAVE OSTHUS[§], SHRIRAM SRINIVASAN[¶],
HARI VISWANATHAN[†], AND GOWRI SRINIVASAN[‖]

Abstract. We present a graph-based method to identify primary flow and transport subnetworks in three-dimensional discrete fracture networks (DFNs). The structure of a DFN lends itself to the use of graphs as a coarse-scale representation that retains the multiscale nature of flow and transport through fracture media. We develop a bipartite graph representation that integrates fracture network topology, fracture geometry, and hydraulic properties. We show that the two most common graph-representations of DFNs, vertices representing intersections and vertices representing fractures, are projections of this bipartite graph thereby providing a generalization of previous DFN-graph frameworks. The primary subnetworks in each DFN are identified by running a heuristic algorithm that determines the edge-disjoint shortest paths through the graph which correspond to the regions where the fastest transport occurs. The method does not have any user-defined parameters and terminates in a finite number of steps. The quality of the method is demonstrated by comparing transport simulations on the identified primary subnetwork and full network, which are in good agreement for early and middle times. These estimates of the first passage times can be achieved with close to an order of magnitude reduction of computational expense using the proposed method.

Key words. subsurface flow and transport, discrete fracture networks, graph theory, bipartite graphs, system reduction

AMS subject classifications. 05C22, 05C40, 05C62, 05C90

DOI. 10.1137/18M1180207

1. Introduction. Fluid flow and the associated transport of dissolved chemicals through fractured media are inherently multiscale phenomena. Individual fractures interconnect to form complicated networks where relevant length scales can span several orders of magnitude [12]. At the largest scale (1×10^3 m), the structure of network. network connectivity [34], fracture orientation [63], and density [29] are the principal controls of solute transport. At a slightly smaller scale (1×10^1 m to 1×10^2 m) there are the fractures themselves where variable aperture [19, 48], boundary conditions (i.e., locations of inflow and outflow within fractures), and stress conditions [39] can

†Computational Earth Science (EES-16), Earth and Environmental Sciences Division, Los Alamos National Laboratory, Los Alamos, NM 87545 (jhyman@lanl.gov, viswana@lanl.gov).
  ‡Computer, Computational, and Statistical Sciences Division, Los Alamos National Laboratory, Los Alamos, NM 87545 (hagberg@lanl.gov).
  §Statistical Sciences (CCS-6), Computer, Computational, and Statistical Sciences Division, Los Alamos National Laboratory, Los Alamos, NM 87545 (dosthus@lanl.gov).
  ¶Computational Earth Science (EES-16), Earth and Environmental Sciences Division, and The Center for Nonlinear Studies, Los Alamos National Laboratory, Los Alamos, NM 87545 (shrirams@lanl.gov).
  ‖Verification and Analysis (XCP-8), X Computational Physics, Los Alamos National Laboratory, Los Alamos, NM, 87545 (gowri@lanl.gov).

all lead to flow channelization within a given fracture. Then there is an even smaller scale $(1 \times 10^{-1}\,\mathrm{m})$ along fracture intersections/traces where complicated flow-fields form [58, 79]. Finally, fluid and chemical interactions with the rock matrix surrounding the fractures happen at the scale of individual pores $(1 \times 10^{-4}\,\mathrm{m})$ [50].

Determining the passage time of solutes transported along with flow through these interconnected fracture networks is critical for a variety of subsurface applications including hydrocarbon extraction [30, 42, 52], environmental restoration of contaminated fractured media [53, 54, 77], CO_2 sequestration [37], and aquifer storage and management [45]. One method to model flow and transport through fractured media is discrete fracture networks (DFNs). In the DFN methodology individual fractures are commonly represented as $(N-1)$-dimensional objects embedded within an N-dimensional space, e.g., lines in two dimensions or planar polygons in three dimensions, and each fracture is assigned a shape, location, and orientation within the domain based on a site characterization. The fractures form an interconnected network embedded within a rock matrix that is considered impermeable. Each fracture is meshed for computation and the governing equations for flow and transport are numerically integrated on the network. Figure 1 shows a steady-state solution for fluid pressure in a three-dimensional DFN composed of 7200 fractures (left), a moderate sized DFN, to highlight the complexity of these simulations.
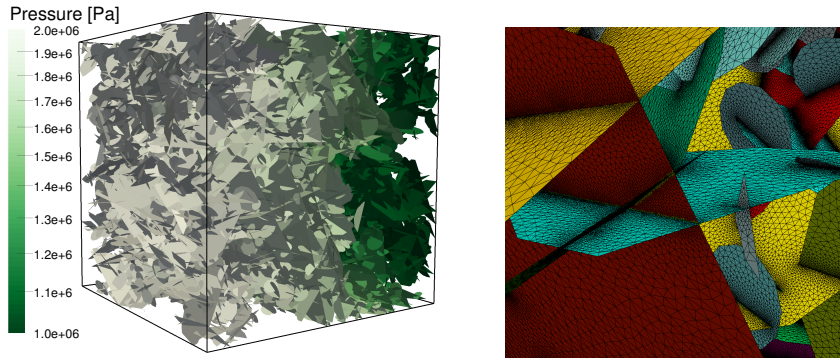

FIG. 1. *A steady-state solution for fluid pressure in a DFN. Left: The DFN is composed of 7200 fractures with a mesh of just under 16 million nodes* [32]. *Right: A close-up of part of the DFN showing details of the conforming Delaunay triangulation.*

The primary advantage of DFN models over conventional continuum models is that network attributes can be linked to observed flow and transport properties. For example, flow channeling, isolated regions of high velocity in fracture media, is commonly observed in field and laboratory experiments and in numerical simulations [1, 2, 19, 23, 61]. This phenomenon indicates the existence of primary subnetworks, also referred to as the network *backbones*, where the fastest transport occurs. Flow and transport simulations in DFNs can be used to link the fracture attributes and network structures to inclusion in the backbone.

The choice to explicitly represent fractures and network structure makes DFN models computationally expensive. Even a modestly sized network, such as the one shown in Figure 1 where the mesh contains nearly 16 million nodes, can require several hours for meshing, flow, and transport simulations even when run in parallel. Because of this high computational expense, the application of DFN models has been limited to one-dimensional pipe-network approximations [15, 20], two-dimensional

systems [17, 18, 16], or relatively small three-dimensional systems [11]. Recent advances in mesh generation [32], discretization techniques [21, 59, 60], and computational frameworks [8, 9] along with advances in high performance computing have made computing in DFN models feasible for larger systems. But even these advances are not sufficient for the widespread usage of DFN simulations. The characteristics of fractures in the subsurface can never be known exactly at a particular field site; therefore, the fracture attributes are assumed to be the result of a stochastic process. For computational models the attributes are sampled from distributions whose parameters are determined by geological site characterizations. This results in the need for an ensemble of computational realizations to bound system uncertainty.

One approach to reduce the computational cost of DFN modeling is the identification of network backbones prior to flow and transport simulations. Once a backbone is identified, meshing and simulations need only be performed on a smaller subnetwork of the whole domain [33]. The objective of finding a backbone consists of maximizing the number of fractures removed from the network while minimizing the error in a quantity of interest, such as the distribution of particle transport times, i.e., the breakthrough curve. This problem of backbone identification for system reduction can be cast as a binary optimization problem where elements, such as fractures or intersections, are either retained or removed. However, attacking this binary optimization problem head-on is infeasible. Whenever a fracture is removed from the network, the entire network needs to be remeshed, a new steady-state pressure solution obtained, and particles tracked through the derived subnetwork. For any DFN of reasonable size, it is impossible to put this idea to practice in a optimization workflow as each iteration can take hours.

To make backbone identification possible, a number of heuristic methods have been developed, each with advantages and disadvantages. Intuition about the fractures that make up backbones can be obtained by using the results of flow and transport to extract network backbones a posteriori. Maillot et al. [47] identified backbones in three-dimensional DFNs by considering the total flux on each fracture plane. They applied a user defined threshold to partition the DFN into primary and secondary regions. Aldrich et al. [4] used particle trajectory information from high-fidelity DFN simulations to create a weighted directed graph representation of the DFN. They identified a backbone hierarchy where fractures are ranked by the amount of mass that passed through them. While these methods do identify network backbones, they require that costly high-fidelity flow simulations be performed first.

Another approach is to classify the properties of the fractures and network structure prior to running flow and transport. Which fractures make up the backbone depends on the macroscale structure of the network, e.g., orientations and density, meso-scale hydrological attributes, e.g., fracture permeability [17, 31], and the boundary conditions [25, 54]. Current methods try to account for these features. For example, a naive approach is to use geometric thresholding, i.e., remove all fractures smaller than a threshold size. These smaller fractures are narrower and have lower permeability and thus the highest resistance to flow. However, backbones tend to be made up of a few larger fractures that are connected together by smaller fractures [31]. Thus, removing all small fractures below a size threshold fails to identify the backbone because it can eliminate primary flow paths, which in turn influences transport properties [78]. Thus, topological properties of the network need to be considered to identify backbones as well.

The structure of a DFN naturally lends itself to the use of graphs as a coarse-scale representation to capture network connectivity. There are multiple ways to represent

a fracture network using a graph, but at its core the graph describes how fractures in the network are related to one another. A variety of research teams have used graphs to query topological structures of fracture networks [5, 27], account for the influence of topology on upscaled properties [24, 64], link flow properties to topological structure [4, 33, 66, 67, 68, 76], and partition a DFN for high performance computing (HPC) simulations [9]. One idea to identify a backbone using graphs is to identify the 2-core of the network (the k-core of a graph is the maximal subgraph that contains vertices of degree k or greater [70]) and remove its complement. Physically, this set corresponds to fractures where transport can enter and exit a fracture through different intersections; all dead-end fractures are recursively removed. In two-dimensional fracture networks, dead-end fractures are no-flow regions and removing them does not influence flow and transport properties, and removing these fractures is a standard preprocessing step [7]. However, in three dimensions these dead-end fractures do contain nonzero flow due to local recirculation caused by pressure gradients along fracture intersections [58] and therefore influence late times in advective transport time distributions. Removing these dead-end fractures prior to flow and transport simulations is inappropriate if long term plume behavior is primarily of interest. Other graph-based methods include finding the union of subgraphs based on the k-shortest loopless paths between source and target vertices, which corresponded to the fewest number of fractures between inflow and outflow boundaries [33], and using supervised machine learning classification algorithms to identify subgraphs using topological features, e.g., betweenness centrality, and fracture features, e.g., permeability [76].

We address the problem of backbone identification using a method that combines high-fidelity DFN simulations with a weighted bipartite graph representation of the DFN. A caricature of the method is shown in Figure 2. Given a DFN F (Figure 2(a)), we use a mapping Φ to create a projection of a weighted bipartite graph, denoted G (yellow nodes and edges in Figure 2(b)),

$$(1) \qquad\qquad\qquad \Phi : F \to G \,.$$

Next, we find the subgraph G',

$$(2) \qquad\qquad\qquad \chi : G \to G'$$

corresponding to the shortest edge-disjoint paths through the graph (black nodes and edges in Figure 2(b)) between inflow and outflow boundaries (red and blue nodes, respectively). Finally, we identify the subnetwork F' that is the preimage of G' (Figure 2(c)),

$$(3) \qquad\qquad\qquad \Phi^{-1} : G' \to F' \,.$$

The goal is that for a given metric $\| \cdot \|$ of a flow and transport observable, such as first arrival time of a passive solute carried along with the flow, or peak arrival time (denoted by an operator L), the difference between F and F' is acceptably small,

$$(4) \qquad\qquad\qquad \|L(F) - L(F')\| < \varepsilon \,,$$

but that the size of the set of removed fractures is as large as possible. The method overcomes the most common limitations in backbone identification methods that require flow and transport simulations or user defined parameters, or that do not consider topological, geometric, and hydrological properties of the DFN.
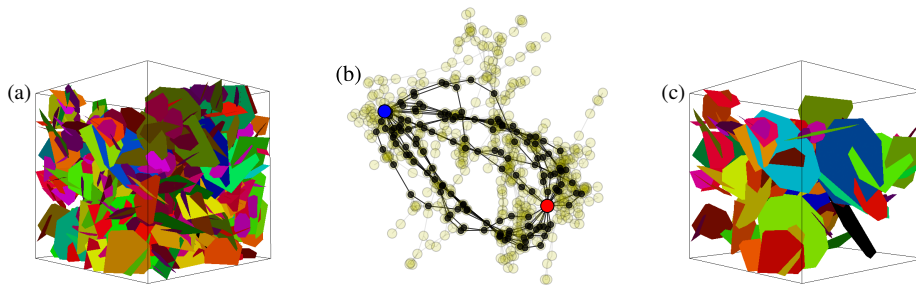
FIG. 2. *An overview of the graph-based method for discrete fracture networks (DFNs).* (a) *A three-dimensional DFN where planes represent fractures in the subsurface.* (b) *A graph representation of the DFN. The black vertices and edges are identified as the primary subgraph for the given source (red) and sink (blue) vertices.* (c) *The DFN backbone corresponding to the subgraph shown in* (b). *(Figure is in color online.)*

The proposed bipartite graph method accounts for the multiscale nature of flow through fractured media. The largest scale of the network structure is retained through the connectivity of the graph, and in-fracture characteristics are captured through edge weights. To identify a network backbone, we implement a heuristic algorithm to find edge-disjoint paths through the graph that correspond to the paths of least resistance through the DFN due to the adopted edge-weighting scheme. We prove that the algorithm terminates in finite time without user defined parameters to determine the size of the backbone, and also provide an estimate of the required computational time. Quality of the method is determined by computing and comparing transport on the backbone subnetworks and the full networks. In particular, we consider the first passage time through each network and the distribution of passage times. First-passage times are in good agreement. The distribution of passage times is in good agreement for early transit times; however, the tails of the travel time distributions exhibit different scaling behaviors. Nonetheless, accurate estimates of the first passage times can be achieved with close to an order of magnitude reduction of computational expense using the proposed method. In addition to the development and exposition of the method, we show that the two most common graph representations of DFNs, namely, vertices representing intersections and vertices representing fractures, are projections of this bipartite graph thereby providing a generalization of previous DFN-graph frameworks.

2. DFN flow and transport. Flow and transport in low-permeability fractured media, granites, shales, and crystalline rocks, is constrained to fractures embedded within the rock matrix at short and medium time scales [53]. In such systems, the geometry of individual fractures, size, and aperture, and the structure of the network are the principal controls of fluid flow as opposed to other properties such as matrix porosity or pore-size distributions. There are a number of methods used to model flow and the associated transport of dissolved chemical species such as stochastic continuum [54], dual-porosity/dual-permeability [46], and DFN.

We focus on the DFN method where individual fractures are represented as planar $(N-1)$-dimensional objects embedded within an N-dimensional space. Because fracture attributes can never be exactly known in the subsurface, the networks are constructed stochastically. Each fracture is assigned a shape, location, and orientation within the domain by sampling distributions whose parameters are determined by a

site characterization. The fractures form a network embedded within an impermeable rock matrix; there is no interaction between flow within the fractures and the solid matrix. Each fracture is meshed for computation, and the governing equations for flow and transport are numerically integrated on the network.

Under the assumption of an incompressible fluid and uniform fracture aperture b, flow through each two-dimensional fracture is equivalent to Poiseuille flow between two parallel plates. Integrating the fluid velocity field in the direction perpendicular to the flow direction reveals that the volumetric flow rate Q per unit fracture width normal to the direction of flow is

$$(5) \qquad Q = \frac{-b^3}{12\mu}\nabla P \,,$$

where μ is the fluid viscosity, and ∇P is the pressure gradient, i.e., the Boussinesq equation [14]. Let $k = b^2/12$ denote permeability, and then we can rearrange terms to arrive at Darcy's law,

$$(6) \qquad \mathbf{q} = -\frac{k}{\mu}\nabla P \,,$$

where $\mathbf{q}$ is the Darcy flux (Q/b). Equation (6) determines the local flow field within each two-dimensional fracture plane.

The boundary conditions within each fracture are determined by the network structure as well as the global boundary conditions. Without loss of generality, we will consider a DFN within a cubic domain of size $L \times L \times L$ with coordinate system (x, y, z) and assume that flow is driven through the network by a pressure gradient aligned with the x-axis of the domain. Dirichlet boundary conditions for the pressure are applied on the x faces ($\mathbf{x_0} = (0, y, z)$ and $\mathbf{x_L} = (L, y, z)$), no-flow boundary conditions are applied along lateral boundaries, and we do not consider the effects of gravity for simplicity. These boundary conditions along with volume conservation,

$$(7) \qquad \nabla \cdot \mathbf{Q} = 0 \,,$$

and (6) are used to form an elliptic partial differential equation for steady-state distribution of pressure within each network,

$$(8) \qquad \nabla \cdot (k\nabla P) = 0 \,.$$

The solution to these governing equations provides values of pressure and volumetric flow rates throughout the entire network that can be used to obtain the Eulerian velocity field $\mathbf{u}(\mathbf{x}) = \mathbf{q}/\phi$ within the DFN [49, 57, 72], where ϕ is the fracture porosity.

Passive transport through the flow field $\mathbf{u}(\mathbf{x})$ within the DFN can be represented using a plume of indivisible nonreactive particles, e.g., using a Lagrangian approach. Since we assumed that the imposed pressure gradient is aligned with the x-axis, the primary direction of flow is the x direction. The set of particle initial positions $\mathbf{a}$ are distributed along intersections of the fractures with the inlet plane $\mathbf{x_0}$. The trajectory $\mathbf{x}(\mathbf{a}; t)$ of a particle starting at $\mathbf{a}$ at time $t = 0$ is given by the advection equation

$$(9) \qquad \frac{d\mathbf{x}(\mathbf{a}; t)}{dt} = \mathbf{v}(\mathbf{a}; t), \qquad\qquad \mathbf{x}(\mathbf{a}; 0) = \mathbf{a} \,,$$

where the Langrangian velocity $\mathbf{v}(t; \mathbf{x})$ is given in terms of the Eulerian velocity $\mathbf{u}(\mathbf{x})$ as

$$(10) \qquad \mathbf{v}(\mathbf{a}; t) = \mathbf{u}[\mathbf{x}(\mathbf{a}; t)] \,.$$

The length of the pathline ℓ is used to parameterize the spatial and temporal coordinates of the particle. Under this formulation, the travel time $\tau(\mathbf{a}, \mathbf{x}_L)$ of a particle that has crossed the outlet plane $\mathbf{x}_L$ of a DFN can be written as

$$(11) \qquad \tau(\mathbf{a}; \mathbf{x}_L) = \int \frac{d\ell}{v[\mathbf{a}; t(\ell)]} \,,$$

where $v(\mathbf{x}) = \|\mathbf{u}(\mathbf{x})\|$ is the Eulerian velocity magnitude.

Along a pathline each particle will pass through numerous fractures. The specific fractures in the pathline are determined by the variable resistance offered by the fracture network which is a function of the local fracture geometry, in-plane intersections, and fracture aperture (equivalently, permeability), as well as global network structure. Darcy's law (see (8)) implies that locally $v(\mathbf{x}) \propto k(\mathbf{x})$; therefore,

$$(12) \qquad \tau(\mathbf{a}, \mathbf{x}_L) \propto \int \frac{d\ell}{k[\mathbf{a}; t(\ell)]} \,.$$

Let $R(\mathbf{x}) = 1/k(\mathbf{x})$ denote hydraulic resistance and we can rewrite the previous equation as

$$(13) \qquad \tau(\mathbf{a}, \mathbf{x}_L) \propto \int R(\mathbf{a}; \ell) d\ell \,.$$

Physically, this integral combines the distance traveled by a particle along with the hydraulic resistance encountered along its pathline. It shows that the travel time of a particle depends upon the internal fracture geometry (length), hydraulic properties (hydraulic resistance), and network structure. Next, we develop a coarse-scale bipartite graph representation of a DFN that accounts for the multiscale nature of fracture networks including these key fracture properties, distance and hydraulic resistance, along with global network structure.

3. Graph representations of DFNs. At the core of the DFN methodology is the conceptual model of a set of fractures, which are discrete entities, intersect with one another to form a network. Let $F = \{f_i\}$ for $i = 1, \ldots, n$ denote a fracture network composed of n fractures, and let $I = \{(f_i, f_j)\}$ be a set of pairs associated with intersections between fractures; if $f_i \cap f_j \neq \emptyset$, then $(f_i, f_j) \in I$. The number of intersections $m = |I|$ depends on the particular shape, orientation, and geometry of the set of fractures in the network. Figure 3 shows an example of the various graph representations of a DFN which we define in this section.

We define a mapping Φ from the fracture network, defined as the tuple (F, I), into a bipartite graph $G = (U, V, E)$ of two disjoint vertex sets $U(G)$ and $V(G)$ with edges $E(G)$ connecting vertices between the two sets. In this mapping, vertices in U correspond to fractures in F,

$$(14) \qquad \Phi : f_i \to u \in U \,,$$

and vertices in V correspond to intersections, I, between fractures in F,

$$(15) \qquad \Phi : f_i \cap f_j \to v \in V \,.$$

Note that the preimage of any vertex $v \in V$ is a pair of fractures in I,

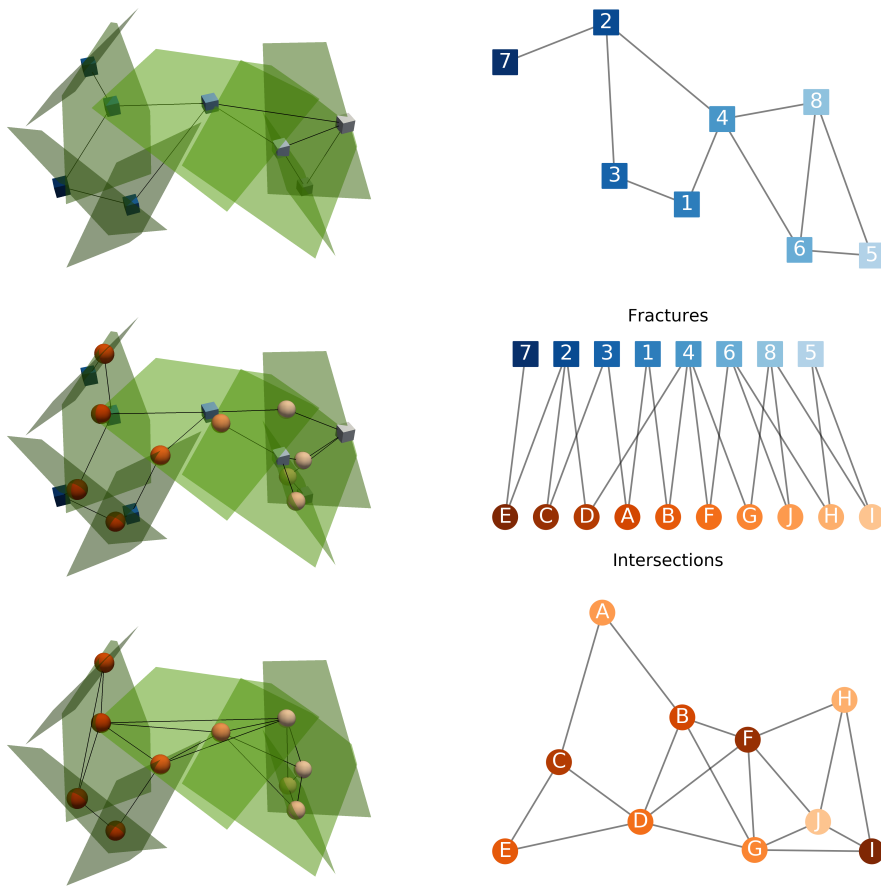$$(16) \qquad \Phi^{-1} : v \to (f_i, f_j).$$

Fig. 3. *Graph representations of a small DFN. On the left is a DFN composed of eight fractures (green planes) with an embedded graph representation. The top row shows the projection onto fracture vertices, indicated as squares, the bottom shows the projection onto intersections vertices, indicated as circles, and the middle row shows the bipartite graph including both fracture and intersection vertices. (Figure is in color online.)*

Edges $e(u, v) \in E$ are defined using the preimages of u and v,

$$(17) \qquad e(u, v) \in E(G) \quad \text{if} \quad \Phi^{-1} : u \in \Phi^{-1} : v.$$

In other words, there is an edge between vertices $u \in U$ and $v \in V$ if the fracture that maps to u is one of those in the intersection that maps to v. Note, as well, that because F and I are finite, G is also finite.

3.1. Bipartite projections. Next, we define additional graphs that are projections of the bipartite graph G onto the vertex sets U and V. These graphs provide convenient representations for developing algorithms for graph reduction in the following sections. The projections are defined using the neighborhood of vertices in the graph.

DEFINITION 3.1. *The neighborhood of a vertex is the set of all adjacent vertices. For $u \in V$ in a graph $G = (V, E)$ the neighborhood $N(u)$ is*

$$(18) \qquad N(u) = \{v \in V(G) \quad s.t. \quad e(u,v) \in E(G)\}\,.$$

DEFINITION 3.2. *The projection of a bipartite graph $G = (U, V, E)$ onto the vertex set U with respect to the vertex set V is the graph $G' = (U, E')$ with $e(u_i, u_j) \in E'$ if $N(u_i) \cap N(u_j) \neq \emptyset$ for u_i and u_j in U.*

3.1.1. Fracture vertex projection. The projection of the bipartite graph G onto the vertices in U is equivalent to the following direct mapping ϕ that transforms F into a graph $G_F = (U, E)$. Let $F = \{f_i\}$ for $i = 1, \ldots, n$ denote a DFN composed of n fractures. For every fracture $f_i \in F$, there is a unique vertex $u_i \in U$,

$$(19) \qquad \phi : f_i \to u_i\,.$$

If two fractures, f_i and f_j, intersect $f_i \cap f_j \neq \emptyset$, then there is an edge in E connecting the corresponding vertices,

$$(20) \qquad \phi : f_i \cap f_j \neq \emptyset \to e_{ij} = (u_i, u_j)\,.$$

THEOREM 3.3. *The mapping ϕ is a bijection between the fractures in F and the vertices in G_F.*

Proof. By construction there is a unique vertex $u \in U$ for every $f \in F$ (see (19)). Thus ϕ is injective. Likewise, for every vertex $u \in U$ there is a unique fracture in F,

$$(21) \qquad \phi^{-1} : u \to f\,.$$

Thus ϕ is also surjective. $\qquad\qquad\qquad\qquad\qquad\qquad\qquad\qquad\qquad\qquad$ □

COROLLARY 3.4. *The projection G_F is isomorphic to F.*

These facts are useful because they ensure that every subgraph

$$G' = (V(G') \subseteq V(G_F), E(G') \subseteq E(G_F))$$

has a unique preimage F' in the fracture network,

$$(22) \qquad \phi^{-1} : G' \to F'\,,$$

that is a subnetwork of the original network, i.e., $F' \subseteq F$. Previous studies have used this graph representation of a DFN to characterize and compare network structure [5, 27] and identify network backbones [4, 33, 76].

3.1.2. Intersection vertex projection. The projection of the bipartite representation G onto the vertices in V gives the graph $G_I = (V, E)$, where the $v \in V$ represent intersections of fractures. This projection is equivalent to the following direct mapping ψ from F to G_I. If two fractures, f_i and f_j, intersect, $f_i \cap f_j \neq \emptyset$, then there is a vertex $v \in V$,

$$(23) \qquad \psi : f_i \cap f_j \to v\,,$$

that represents the line of intersection between the fractures f_i and f_j. If $f_i \cap f_j \neq \emptyset$ and $f_i \cap f_k \neq \emptyset$, then there is an edge in E connecting the corresponding vertices,

$$(24) \qquad \psi : f_i \cap f_j \neq \emptyset \quad \text{and} \quad f_i \cap f_k \neq \emptyset \to e(u, v) \in E(G_I)\,.$$

Under the mapping ψ each fracture is represented by a k-clique where k is the number of intersections on the fracture. Thus, each edge can be thought of as residing on a single fracture, and edge weights can represent hydrological and geometric properties of that fracture. Unlike ϕ, ψ is not a bijective mapping between the fractures in F and $G_I(V, E)$, because it is not surjective. However, subnetworks F' that correspond to subgraphs $G' = (V(G') \subseteq V(G_I), E(G') \subseteq E(G_I))$ can be obtained by using projections of subgraphs of the bipartite representation G. This representation can be used as a coarse-scale domain for flow and transport simulations [43, 56] similar to the conventional equivalent pipe-network model for DFN [15, 20, 55].

3.2. Graph representations of flow problems. Flow problems in a DFN specify inflow and outflow boundaries, and we must capture that information in our graph representation. To do so, we begin by adding source and target vertices, denoted s and t, respectively, into the set of vertices $U(G)$ using the following rules:

1. If a fracture f_i intersects the inlet plane by $(\mathbf{x}_0)$, then a vertex v is added to V, which corresponds to the line of intersection between f_i and $\mathbf{x}_0$, and an edge between the vertex u corresponding to f_i and v is added to E, and another edge that connects v with s is also added to E.
   (25)
   If $f_i \cap \mathbf{x}_0 \neq \emptyset$, then $\exists\, v \in V$ and $\exists\, e(u, v)$ and $e(v, s) \in E$, where $\Phi^{-1} : u \to f_i$.

2. If a fracture f_i intersects the outlet plane by $(\mathbf{x}_L)$, we add a vertex v to V that corresponds to the line of intersection of the f_i with $\mathbf{x}_L$. Then there is an edge between the vertex in u corresponding to f_i and v and another edge that connects v with t.
   (26)
   If $f_i \cap \mathbf{x}_L \neq \emptyset$, then $\exists\, v \in V$ and $\exists\, e(u, v)$ and $e(v, t) \in E$, where $\Phi^{-1} : u \to f_i$.

When considering the projection G_I, it is convenient to think of the set of vertices with an edge to s as a single vertex and likewise for t. We will use the notation $\hat{s} = \{v \mid e(v, s) \in E(G_I)\}$ and $\hat{t} = \{v \mid e(v, t) \in E(G_I)\}$ and treat them as single vertices in G_I.

4. Identifying backbones with an edge-disjoint path algorithm. For our goal of identifying the subnetwork where the fastest transport occurs, we find the path of least resistance through a network. Recall that the projection of G onto vertices in V (the graph G_I) is a coarse-scale representation of the DFN where cliques in G_I correspond to individual fractures in F and geometric properties of the fractures, such as length between intersections and hydraulic resistance, are represented as edge weights $w(u, v)$. Thus, we can consider a particle traveling through G_I from vertex to vertex as a proxy for transport through F. Equation (13) implies that the resistance along a pathline is a function of internal fracture geometry (length) and hydraulic properties (hydraulic resistance). Thus, along a given edge $e(u, v) \in E(G_I)$ the travel time $\tau(u, v)$ for a particle to move from vertex u to v should scale according to the same behavior as in the DFN,

$$(27) \qquad\qquad \tau(u, v) \propto R(u, v) \times l(u, v) \ ,$$

where $l(u, v) = \|u(\mathbf{x}) - v(\mathbf{x})\|$ is a measure of distance between the line of intersection represented by the vertex u and v (here we take $u(\mathbf{x}) \in \mathbb{R}^3$ to be the center of the intersection line) and $R(u, v) = 1/k(u, v)$ is the hydraulic resistance on that particular fracture. Using this construction, we can consider a path $p = \{(u, v)\}$ from source $\hat{s}$

to target $\hat{t}$, and the total travel time of the particle scales according to the sum of $\tau(u, v)$ along p,

$$(28) \qquad\qquad \tau(\hat{s}, \hat{t}) \propto \sum_{(u,v) \in p} R(u, v) \times l(u, v) \ .$$

Therefore, the fastest transport in the DFN should occur along fractures that are the preimage of the shortest paths through the graph G_I from $\hat{s}$ to $\hat{t}$ where edge weights are $w(u, v) = R(u, v) \times l(u, v)$. Note that these weights are a combination of geometry and physical attributes of each fracture, and use of paths from $\hat{s}$ to $\hat{t}$ accounts for the global network structure. Identifying paths of least resistance and linking them to the fastest transport has also been performed in two- and three-dimensional heterogeneous porous media [62, 75]. In many natural media permeability is well described by a log-normal distribution [65]. To partially account for this we consider $\ln R$ rather than R. Note that this means the dimensions of this weighting scheme are length.

4.1. Computing edge-disjoint paths. Next, we need to identify the n-shortest weighted loopless paths in G_I from $\hat{s}$ to $\hat{t}$. The presence of cliques in G_I complicates the direct application of this idea. The cliques represent multiple pathways on individual fractures in the DFN. As the number of shortest paths n increases, computing simple shortest paths uncovers permutations of the edges within cliques. Note that this issue does not occur in two-dimensional DFNs because the graph representation G_I there is not composed of cliques. Since the union of these paths does not include additional edges other than the clique edges, the preimage in the fractures F does not grow. This problem is resolved by considering edge-disjoint shortest paths from the source to target; two paths in a graph are *edge-disjoint* if they do not share an edge.

There are several types of edge-disjoint path problems. The one most studied is the edge-disjoint path problem for multiple pairs of source and target vertices. However, we have a simpler problem of considering only a single pair of source and target vertices. Another distinguishing feature of our setup from the standard edge-disjoint shortest path problem is that we do not seek to minimize the sum of disjoint path lengths between source and target [10, 71, 73, 74]. Implementing algorithms designed for shortest path sum can identify sets of disjoint paths that do not include the shortest path [10], which can eliminate the subgraph corresponding to the sub-network where the fastest transport occurs.

Based on our requirements for DFN flow problems we select a different method than those typically used for edge-disjoint shortest path problems. We implement a greedy method which identifies a subgraph G' by sequentially finding the weighted shortest edge-disjoint paths from the source to the target. The details are presented in Algorithm 1.

Menger's theorem [51] implies that the number of edge-disjoint paths from s to t is the minimum edge cut k of the graph G between s and t. Because the graph is finite, k is also finite. A direct result of this is the following.

THEOREM 4.1. *The required time for the method is $O(k(m + n))$.*

Proof. For a graph G with n vertices and m edges the weighted shortest path set can be computed using breadth-first search in $O(m + n)$ time [69]. This fact, along with Menger's theorem, providing the maximum number of edge-disjoint paths is k, implies that the required time for the method is $O(k(m + n))$. $\qquad\square$

COROLLARY 4.2. *The algorithm finishes in finite time.*

Algorithm 1. Greedy algorithm for edge-disjoint subgraph of G.

Input: $G = (V, E)$ with $s, t \in V$ and weights $w(u, v)$ on edges $(u, v) \in E$
Output: $G' = (V, E)$ with $V(G') \subseteq V(G), E(G') \subseteq E(G)$

  $G' \leftarrow \emptyset$ $\triangleright$ Create an empty graph G'
  while $\exists \, s, t\text{-path} \in G$ **do**
    $p \leftarrow$ shortest s, t-path with edge weights $w(u, v)$
    for $(u, v) \in p$ **do**
      $G' \leftarrow G' \cup (u, v)$ $\triangleright$ Add edges from shortest path into G'
      $G \leftarrow G \setminus (u, v)$ $\triangleright$ Remove edges in the shortest path from G
    end for
  end while

Therefore, the method terminates without user defined parameters. This key feature distinguishes the method from other available graph-based methods to find primary subnetworks in DFNs [4, 33, 76].

Once the subgraph G'_I has been identified the associated subnetwork F' must be extracted from the full network. Recall, however, that G_I is not isomorphic to F but G_F is isomorphic to F (Corollary 3.4). Therefore, we first project G'_I onto G_F to obtain G'_F and then use ϕ^{-1} to uniquely determine F'. Note that the subnetwork F' is guaranteed to connect inflow and outflow boundaries because $\hat{s}$ and $\hat{t}$ are connected in G'_I.

5. Application and exposition of the method. We demonstrate the effectiveness of the method for identifying network backbones in fracture networks by applying it to two different DFN scenarios. In the first scenario, we fix the network geometry and vary the hydraulic properties. This scenario is meant to test the robustness of the method when the primary uncertainty in the system is hydraulic properties rather than geometric or topological, e.g., a system with a narrow range of length scales of fracture size but widely variable apertures. In the second scenario, we generate a set of 100 independent, identically distributed realizations using the same generation parameters. This scenario tests the robustness of the method when the primary uncertainty in the network is geometric and topological, e.g., a fractured media with a wide range of fracture sizes.

Generation, meshing, flow, and transport of each DFN is performed using the DFNWORKS computational suite [35]. The feature-rejection algorithm for meshing (FRAM) [32] is used to generate a Delaunay triangulation that conforms to fracture intersections. The mesh is refined close to fracture intersections to properly resolve large gradients in the pressure solutions that occur in these regions due to points of singularity at intersections tips. The dual mesh of the Delaunay triangulation, the Voronoi diagram, is in a particular sense optimal for two-point flux finite volume codes. On that mesh of Voronoi control volumes, we compute the steady-state pressure field and then derive the flow solution within the fracture network. The parallelized subsurface flow and reactive transport code PFLOTRAN [46] is used to numerically integrate the governing equations for flow described in section 2 to compute the steady-state pressure field using a two-point flux finite volume scheme. The velocity field $\mathbf{u}(\mathbf{x})$ within the DFN is obtained from the resulting pressure field using the method presented in [49, 57], and particle tracking is performed using DFNTRANS [49]. Complete mixing is used to determine what direction particles exit out of fracture intersections [40, 49]. Since we consider passive transport, particles do not interact

with the matrix, i.e., matrix diffusion and sorption are not considered. We use the NETWORKX graph software package [26] for graph representation and to compute each weighted shortest path.

The accuracy of the method is determined by comparing the particle passage times in the original network with those in the identified subnetworks. For each network F and subnetwork F', we consider the relative solute mass flux across the outlet plane,

$$(29) \qquad \Pi(t) = 1/M \int d\Omega \; m(\mathbf{a})\delta[t - \tau(\mathbf{x}_L; \mathbf{a})] \,,$$

where $M = \int d\Omega m(\mathbf{a})$ is the total mass of all particles, $\tau(\mathbf{x}_L; \mathbf{a})$ is defined in (11), and $\Omega = \{\mathbf{a}\}$ is the set of all initial positions in F. Particle mass is variable and is distributed using flux-weighting [44]. We also consider the first passage time of all particles in each network,

$$(30) \qquad \hat{\tau}(F) = \inf_t \{\Pi(t) > 0\} \,.$$

5.1. Scenario 1: Static network geometry with variable hydraulic properties. The first network is composed of 538 square fractures with sides of length $1\,\mathrm{m}$ in a cubic domain with sides of $5\,\mathrm{m}$. Fracture centers are uniformly distributed throughout the domain and normal vectors of the fractures are also uniformly random; there is no preferred fracture orientation. The network intensity, the fracture surface area over total volume P_{32}, is $6.54\,\mathrm{m}^{-1}$. The permeability of each fracture is an independent, identically distributed random variable sampled from a log-normal distribution with mean μ_k and log variance $\sigma_{\ln k}^2$ [65]. We fix $\mu_k = 1 \times 10^{-12}\,\mathrm{m}^2$ and consider three values of $\sigma_{\ln k}^2 = (0.5, 1, 1.5)$, which are moderate levels of hydraulic heterogeneity. To consider the influence of uncertainty of hydrological properties, we create 30 independent permeability realizations for each value of $\sigma_{\ln k}^2$.

Each DFN is reduced using the bipartite graph algorithm to identify the graph backbone. The resulting subnetworks are substantially smaller than the original network. Close to 70% of fractures in static networks are removed for all values of $\sigma_{\ln k}^2$. As a result, the surface areas and mesh sizes are also much smaller with typical reductions of about 70% for both. In turn, the simulations run in about three minutes compared to 10 minutes for the original network.

Figures comparing transport at different levels of $\sigma_{\ln k}^2$ are presented in Figure 4: (top) $\sigma_{\ln k}^2 = 0.5$, (middle) $\sigma_{\ln k}^2 = 1.0$, (bottom) $\sigma_{\ln k}^2 = 1.5$. The scatter plots (left) compare $\hat{\tau}$ (abscissa) and $\hat{\tau}'$ (ordinate). Time has been nondimensionalized by the peak breakthrough time (maximum) of $\Pi(t)$ in the aggregate breakthrough of the original networks. We compute the coefficient of determination (R^2) to examine linear correlation and root mean squared error (RMSE) to quantify error between the values of $\hat{\tau}(F)$ and $\hat{\tau}(F')$. The distributions of travel times (images in the right column) compare transport through the original network (black line) and the subnetworks identified using the bipartite graph method (blue line). Solid lines are the aggregate of all 30 realizations, and dashed gray lines are the 95% confidence interval (CI) envelope for the original networks to show variability in the ensemble. For $\sigma_{\ln k}^2 = 0.5$, the aggregate curves match well for the initial breakthrough and the peak, as the aggregate subnetwork breakthrough curve falls within the 95% CI envelope for the original network but deviate at later times, exiting the 95% CI envelope. The prediction of $\hat{\tau}$ is also good, having a low RMSE and high R^2 values. Similar behavior is observed for $\sigma_{\ln k}^2 = 1.0$ and $\sigma_{\ln k}^2 = 1.5$ and there is more variations between realizations. The subnetwork breakthrough curves are always within the 95% CI envelope for early and

peak times. Only at late times and low densities are the subnetwork breakthrough curves outside the 95% CI envelope. As the variance increases, the predictions of $\hat{\tau}$ exhibit more scatter, indicated by higher RMSE values.
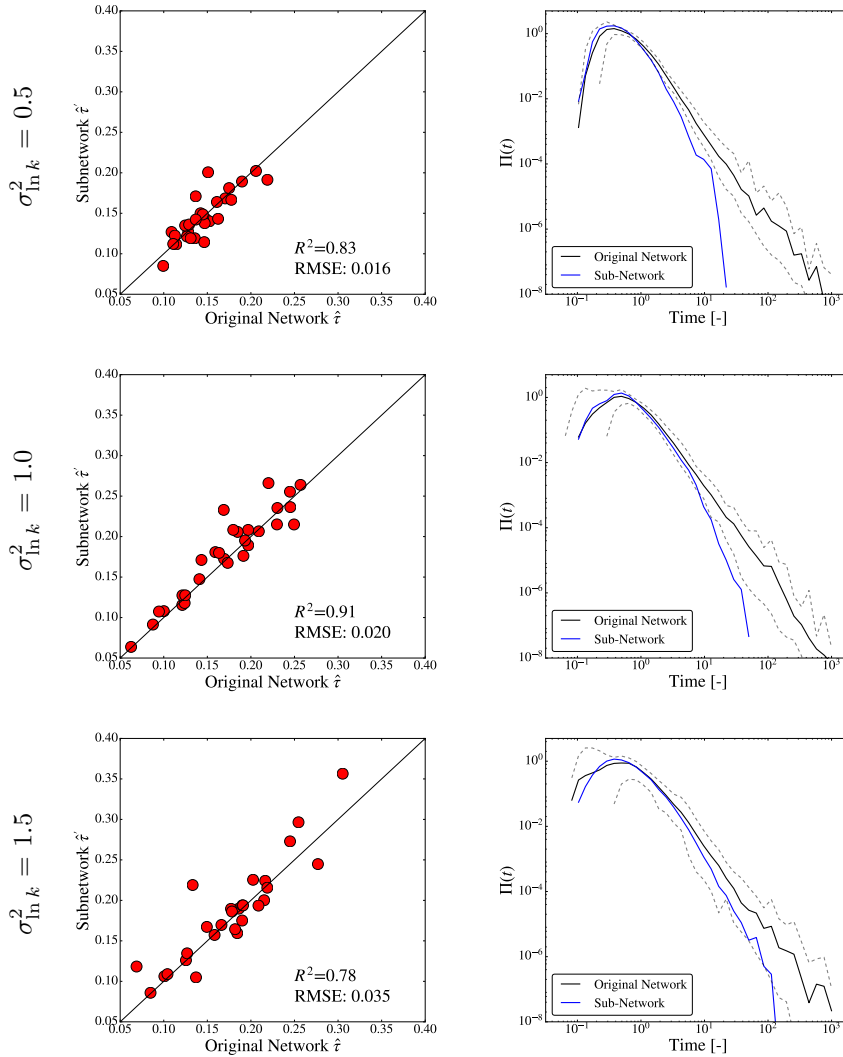

FIG. 4. *Comparison of travel time distributions in the uniform-sized fracture network. The aggregate breakthrough curves $\Pi(t)$ at different levels of $\sigma^2_{\ln k}$ are presented as follows. Top: $\sigma^2_{\ln k} = 0.5$, middle: $\sigma^2_{\ln k} = 1.0$, bottom: $\sigma^2_{\ln k} = 1.5$. Black lines are generated by transport through the original network and blue lines through the subnetworks identified using the proposed method. Each solid line is the aggregate of the 30 realizations. Dashed gray lines are the 95% CI envelope for the original networks to show variability in the ensemble. Time has been nondimensionalized by the peak breakthrough time (maximum) of $\Pi(t)$ for the original networks. The insets compare values of $\hat{\tau}(F')$ plotted against $\hat{\tau}(F)$. In terms of network size, the subnetworks are all around 70% smaller than the full networks both in terms of number of fractures and mesh size, which results in an order of magnitude reduction in run times.*

The good match between first arrival times and early/peak breakthrough times for subnetworks and the full networks indicates that the proposed method does a good

job of identifying the primary subnetworks as the permeability field changes between realizations while keeping network geometry fixed. As the variability of the permeability field becomes larger, its influence on transport properties is more pronounced. Because the method is sensitive to these changes, it provides good estimates of the particle breakthrough. Other purely topological methods for backbone identification [33] are not able to capture such scenarios.

5.2. Scenario 2: Ensemble of networks with the same statistical properties. For this scenario we construct a set of 100 networks with fracture lengths drawn from a powerlaw distribution (the most commonly observed network type in the natural world [12]). Each DFN is constructed in a cubic domain with sides of length 15 m and is composed of circular fractures with uniformly random orientations and uniformly random centers. The range of fracture sizes in this example (radii r [m]) is sampled from a truncated powerlaw distribution with exponent $\alpha = 2.6$ and upper and lower cutoffs ($r_u = 5$ m; $r_0 = 1$ m), with a probability density function of

$$(31) \qquad p_r(r) = \frac{\alpha}{r_0} \frac{(r/r_0)^{-1-\alpha}}{1 - (r_u/r_0)^{-\alpha}}.$$

The connected network density [19] is about 10 times the critical percolation value [13] indicating that networks are sufficiently dense such that there are multiple paths between the inflow and outflow boundaries, but the networks are also fairly sparse (average $P_{32} = 1.97$ m^{-1}). Variability in hydraulic properties is included in the network by correlating fracture apertures to their radii as in [11, 18, 22, 31, 36, 38, 78]. We use a positively correlated powerlaw relationship $b = \gamma r^\beta$, where $\gamma = 5.0 \times 10^{-5}$ and $\beta = 0.5$ are dimensionless parameters. A result of this relationship is that the fracture permeability is also positively correlated to fracture size; larger fractures have higher permeability values. The permeability distributions have lower variance than the networks considered in scenario 1.

The application of Algorithm 1 to reduce the DFN removes over 80% of the network by fracture count, but only 60% by surface area (and 75% of the mesh cells). These values imply that the backbones in the powerlaw networks are primarily made of large fractures. Recall that the hydraulic resistance is inversely correlated to fracture size, i.e., larger fractures have lower hydraulic resistance. Therefore, these subnetworks are geometrically direct paths that also provide low resistance to flow. These features make physical sense and are properties to which the method is sensitive. This reduction in system size results in subnetworks where the simulations run in about four minutes compared to 30 minutes for the original network.

Figure 5 (left) shows one-to-one comparisons of the first passage times in subnetworks versus the first passage time through the full network for scenario 2. Time has been nondimensionalized by the peak breakthrough time in the original networks. The first passage times $\hat\tau$ are in good agreement with R^2 value of 0.96 and RMSE of 1%. In general, however, the subnetworks do predict slightly earlier first arrival times than the original network, a feature which increases with later arrival times in the original networks.

Figure 5 (right) shows the breakthrough curves $\Pi(t)$ (see (29)) for the original network (black line) and the subnetworks (blue line). The values shown are the aggregate of all 100 networks, and dashed gray lines show variability in the ensemble as the 95% CI envelope for the original networks. Transport through the subnetworks matches values of $\Pi(t)$ for early arrival times and the peak within the 95% CI envelope. The distributions in the full network and subnetworks both exhibit powerlaw scaling

in the tails of their distributions $\Pi(t) \propto t^{-\beta}$, but the exponents β are different. The full network has an exponent of $\beta \approx -2.6$ while the backbones have a slightly larger value $\beta \approx -4$.
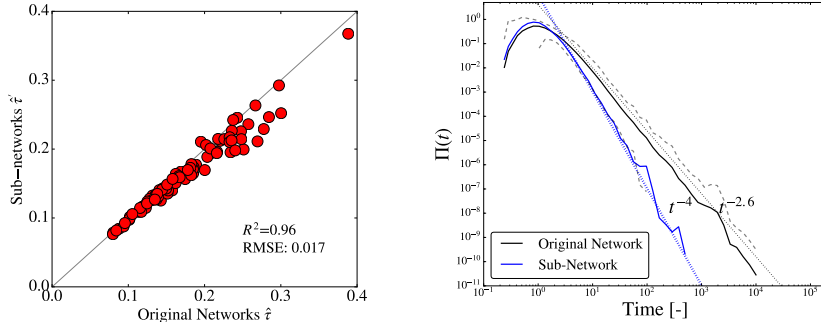

FIG. 5. *Left: First-passage times in subnetworks versus the first passage time through the full network. Time has been nondimensionalized by the peak breakthrough of the ensemble of particle through all 100 networks. The values predicted by the subnetworks are in good agreement with the original networks. Right: Breakthrough curves: $\Pi(t)$ (see (29)) for the original network (black line) and the subnetworks (blue line); dashed gray lines are the 95% CI envelope for the original networks to show variability in the ensemble. Transport through the subnetworks matches values of $\Pi(t)$ for early arrival times as well as the peak, being within the 95% CI envelope. (Figure is in color online.)*

6. Discussion. We have presented a graph-based multiscale method to identify the subnetworks that correspond to the paths of least resistance through three-dimensional fracture networks. The approach uses a bipartite graph to represent the fracture networks and account for key topological, geometric, and hydrological properties, which unifies the two most common graph representations of DFNs, namely, vertices representing intersections and vertices representing fractures, which are projections of this bipartite graph thereby providing a generalization of previous DFN-graph frameworks. The method determines a subgraph based on the union of shortest edge-disjoint paths from source to target, finishes in finite time, and has no user defined parameters. We show that the adopted bipartite-graph representation provides some key properties that link the coarse-scale graph and fine-scale DFN. Specifically, the isomorphism between the projection of the graph onto the vertices, which correspond to fractures, and the fracture networks allows for the unique identification of sub-networks based on subgraphs. Moreover, the projection onto the vertices, which corresponds to intersections in the DFN, allows geometric and hydrological properties of the fracture networks into the graphs as edge weights.

The weighting scheme for the graph edges is based on estimates of particle travel times and the subgraphs obtained using the algorithm correspond to subnetworks where the fastest transport occurs. The quality of the method is demonstrated by comparing first passage time distributions on two different test sets of fracture networks. The first is a DFN composed of uniform-sized square fractures with varying degrees of hydraulic heterogeneity, and the second is a set of 100 independent DFNs composed of fractures whose radii are drawn from a powerlaw distribution. In all cases considered we found that the breakthrough curves of the subnetworks are in good agreement with the original networks for early and peak times. However, they deviate at later times and produce different powerlaw scaling behavior. The latter is expected because late time arrival in fracture networks is controlled by fractures that

are not in the network backbone. As previously mentioned, edge weights are based on estimates of particle travel times which is key to identifying the subnetworks where the fastest transport occurs. If one would like to use the algorithm to identify subnetworks that retain other properties of the original DFN, e.g., permeability or late time arrival, then other weighting schemes would need to be considered.

These system reductions result in close to an order of magnitude reduction in the required computing times for meshing, flow, and transport simulations on modest-sized networks. The subnetworks contain significantly fewer fractures to mesh, which results in fewer degrees of freedom in the linear system for the pressure and faster convergence of the solver. The time required for transport is also reduced because a smaller number of fractures intersect the inlet plane and thus fewer particles are inserted into the domain.

While we have focused primarily on DFN, the method of backbone identification could also be of use in discrete fracture matrix (DFM) models [3, 6, 28, 41], where a flow and transport matrix is considered along with that in the DFN. Considering only the network backbone in a DFM would reduce the degrees of freedom and possibly simplify the coupling between the fracture and the surrounding matrix.

In comparison to the other algorithms available to identify primary subnetworks, e.g., Aldrich et al. [4], Hyman et al. [33], and Maillot et al. [47], the proposed method has a few key advantages. The methods proposed by Maillot et al. [47] and Aldrich et al. [4] both require solving flow and transport through the entire DFN prior to backbone identification along with postprocessing of the solutions. From a computational point of view, therefore, these methods are far more expensive. While the method proposed in Hyman et al. [33] does not suffer from these limitations, it does not take into account the network geometry or physical properties such as permeability. Considering the first validation example where the network is fixed and fracture permeabilities are sampled from a log normal distribution, section 5.1, the method of Hyman et al. [33] will return the same subnetwork for every realization of the permeability field and is therefore less robust. Moreover, all three of these methods have tuning parameters to determine what is in the backbone and what is not, which is another disadvantage.

However, the method is not without limitations. Although this method provides good estimates of first passage times, advances can still be made if a focus on characteristics of the breakthrough curve at later times is required. To do so, however, one needs to move past considering only shortest paths in the graph representations. Other graph topological properties such as modularity, centrality, and betweenness might also be considered for more global measures of flow connectivity. While the algorithm will always terminate in finite time and return a subgraph, flow and transport properties are not proven to match those of the original DFN. Thus, in practice, one should always simulate transport through at least one of the original DFNs to ensure that flow and transport through the identified backbones are exhibiting the expected behavior. Moreover, the inclusion of both source and target vertices requires that there be clearly defined inflow and outflow locations in the network. However, this is only the case in a subset of DFN scenarios. In many problems, there might only be a unique inflow or outflow, e.g., hydraulic fracturing models where there is a single horizontal well for production [42], or there are multiple sources (injection wells) and multiple sinks (production wells), e.g., geothermal extraction and naturally fractured hydrocarbon reservoirs. While the proposed methodology cannot be applied directly to these scenarios, it could be possible to develop extensions of the method to address such situations and warrants further investigation.

REFERENCES

[1] H. Abelin, L. Birgersson, L. Moreno, H. Widén, T. Ågren, and I. Neretnieks, *A large-scale flow and tracer experiment in granite: 2. Results and interpretation*, Water Resour. Res., 27 (1991), pp. 3119–3135.

[2] H. Abelin, I. Neretnieks, S. Tunbrant, and L. Moreno, *Final Report of the Migration in a Single Fracture: Experimental Results and Evaluation*, Nationale Genossenschaft für die Lagerung Radioaktiver Abfälle, Baden, Switzerland, 1985.

[3] R. Ahmed, M. G. Edwards, S. Lamine, B. A. Huisman, and M. Pal, *Control-volume distributed multi-point flux approximation coupled with a lower-dimensional fracture model*, J. Comput. Phys., 284 (2015), pp. 462–489.

[4] G. Aldrich, J. D. Hyman, S. Karra, C. W. Gable, N. Makedonska, H. Viswanathan, J. Woodring, and B. Hamann, *Analysis and visualization of discrete fracture networks using a flow topology graph*, IEEE Trans. Vis. Comput. Graph, 23 (2017), pp. 1896–1909.

[5] C. A. Andresen, A. Hansen, R. Le Goc, P. Davy, and S. M. Hope, *Topology of fracture networks*, Front. Phys., 1 (2013), 7.

[6] P. F. Antonietti, L. Formaggia, A. Scotti, M. Verani, and N. Verzott, *Mimetic finite difference approximation of flows in fractured porous media*, ESAIM Math. Model. Numer. Anal., 50 (2016), pp. 809–832.

[7] B. Berkowitz and H. Scher, *Theory of anomalous chemical transport in random fracture networks*, Phys. Rev. E, 57 (1998), pp. 5858–5869, https://doi.org/10.1103/PhysRevE.57.5858.

[8] S. Berrone, S. Pieraccini, and S. Scialo, *A PDE-constrained optimization formulation for discrete fracture network flows*, SIAM J. Sci. Comput., 35 (2013), pp. B487–B510, https://doi.org/10.1137/120865884.

[9] S. Berrone, S. Pieraccini, S. Scialò, and F. Vicini, *A parallel solver for large scale DFN flow simulations*, SIAM J. Sci. Comput., 37 (2015), pp. C285–C306, https://doi.org/10.1137/140984014.

[10] R. Bhandari, *Optimal physical diversity algorithms and survivable networks*, in Proceedings of the Second IEEE Symposium on Computers and Communications, IEEE, Piscataway, NJ, 1997, pp. 433–441.

[11] I. Bogdanov, V. Mourzenko, J.-F. Thovert, and P. Adler, *Effective permeability of fractured porous media with power-law distribution of fracture sizes*, Phys. Rev. E, 76 (2007), 036309.

[12] E. Bonnet, O. Bour, N. E. Odling, P. Davy, I. Main, P. Cowie, and B. Berkowitz, *Scaling of fracture systems in geological media*, Rev. Geophys., 39 (2001), pp. 347–383.

[13] O. Bour and P. Davy, *Connectivity of random fault networks following a power law fault length distribution*, Water Resour. Res., 33 (1997), pp. 1567–1583.

[14] J. Boussinesq, *Mémoire sur l'influence des frottements dans les mouvements réguliers des fluids*, J. Math. Pures Appl., 13 (1868), pp. 377–424.

[15] M. C. Cacas, E. Ledoux, G. De Marsily, A. Barbreau, P. Calmels, B. Gaillard, and R. Margritta, *Modeling fracture flow with a stochastic discrete fracture network: Calibration and validation: 2. The transport model*, Water Resour. Res., 26 (1990), pp. 491–500.

[16] J.-R. de Dreuzy, C. Darcel, P. Davy, and O. Bour, *Influence of spatial correlation of fracture centers on the permeability of two-dimensional fracture networks following a power law length distribution*, Water Resour. Res., 40 (2004), W01502.

[17] J.-R. de Dreuzy, P. Davy, and O. Bour, *Hydraulic properties of two-dimensional random fracture networks following a power law length distribution 2. Permeability of networks based on lognormal distribution of apertures*, Water Resour. Res., 37 (2001), pp. 2079–2095.

[18] J.-R. de Dreuzy, P. Davy, and O. Bour, *Hydraulic properties of two-dimensional random fracture networks following power law distributions of length and aperture*, Water Resour. Res., 38 (2002), 1276.

[19] J.-R. de Dreuzy, Y. Méheust, and G. Pichot, *Influence of fracture scale heterogeneity on the flow properties of three-dimensional discrete fracture networks*, J. Geophys. Res.-Sol. Ea., 117 (2012), B11207.

[20] W. Dershowitz and C. Fidelibus, *Derivation of equivalent pipe network analogues for three-dimensional discrete fracture networks by the boundary element method*, Water Rescour. Res., 35 (1999), pp. 2685–2691.

[21] J. Erhel, J.-R. de Dreuzy, and B. Poirriez, *Flow simulation in three-dimensional discrete fracture networks*, SIAM J. Sci. Comput., 31 (2009), pp. 2688–2705, https://doi.org/10.1137/080729244.

[22] A. FRAMPTON AND V. CVETKOVIC, *Inference of field-scale fracture transmissivities in crystalline rock using flow log measurements*, Water Resour. Res., 46 (2010), W11502.

[23] A. FRAMPTON AND V. CVETKOVIC, *Numerical and analytical modeling of advective travel times in realistic three-dimensional fracture networks*, Water Resour. Res., 47 (2011), W02506.

[24] H. GHAFFARI, M. NASSERI, AND R. YOUNG, *Fluid Flow Complexity in Fracture Networks: Analysis with Graph Theory and LBM*, preprint, https://arxiv.org/abs/1107.4918, 2011.

[25] P. GRINDROD AND M. IMPEY, *Channeling and Fickian dispersion in fractal simulated porous media*, Water Resour. Res., 29 (1993), pp. 4077–4089.

[26] A. A. HAGBERG, D. A. SCHULT, AND P. SWART, *Exploring network structure, dynamics, and function using NetworkX*, in Proceedings of the 7th Python in Science Conferences (SciPy 2008), 2008, pp. 11–16.

[27] S. M. HOPE, P. DAVY, J. MAILLOT, R. LE GOC, AND A. HANSEN, *Topological impact of constrained fracture growth*, Front. Phys., 3 (2015), p. 75.

[28] M.-H. R. HUI, M. KARIMI-FARD, B. MALLISON, AND L. J. DURLOFSKY, *A general modeling framework for simulating complex recovery processes in fractured reservoirs at different resolutions*, SPE J., 23 (2018), pp. 598–613.

[29] O. HUSEBY, J. F. THOVERT, AND P. M. ADLER, *Dispersion in three-dimensional fracture networks*, Phys. Fluids, 13 (2001), pp. 594–615.

[30] J. HYMAN, J. JIMÉNEZ-MARTÍNEZ, H. S. VISWANATHAN, J. W. CAREY, M. L. PORTER, E. ROUGIER, S. KARRA, Q. KANG, L. FRASH, L. CHEN, Z. LEI, D. O'MALLEY, AND N. MAKEDONSKA, *Understanding hydraulic fracturing: A multi-scale problem*, Phil. Trans. R. Soc. A, 374 (2016), 20150426.

[31] J. D. HYMAN, G. ALDRICH, H. VISWANATHAN, N. MAKEDONSKA, AND S. KARRA, *Fracture size and transmissivity correlations: Implications for transport simulations in sparse three-dimensional discrete fracture networks following a truncated power law distribution of fracture size*, Water Resour. Res., 52 (2016), pp. 6472–6489, https://doi.org/10.1002/2016WR018806.

[32] J. D. HYMAN, C. W. GABLE, S. L. PAINTER, AND N. MAKEDONSKA, *Conforming Delaunay triangulation of stochastically generated three dimensional discrete fracture networks: A feature rejection algorithm for meshing strategy*, SIAM J. Sci. Comput., 36 (2014), pp. A1871–A1894, https://doi.org/10.1137/130942541.

[33] J. D. HYMAN, A. HAGBERG, G. SRINIVASAN, J. MOHD-YUSOF, AND H. VISWANATHAN, *Predictions of first passage times in sparse discrete fracture networks using graph-based reductions*, Phys. Rev. E, 96 (2017), 013304, https://doi.org/10.1103/PhysRevE.96.013304.

[34] J. D. HYMAN AND J. JIMÉNEZ-MARTÍNEZ, *Dispersion and mixing in three-dimensional fracture networks: Nonlinear interplay between structural and hydraulic heterogeneity*, Water Resour. Res., 54 (2018), pp. 3243–3258.

[35] J. D. HYMAN, S. KARRA, N. MAKEDONSKA, C. W. GABLE, S. L. PAINTER, AND H. S. VISWANATHAN, *dfnWorks: A discrete fracture network framework for modeling subsurface flow and transport*, Comput. Geosci., 84 (2015), pp. 10–19.

[36] J. D. HYMAN, S. L. PAINTER, H. VISWANATHAN, N. MAKEDONSKA, AND S. KARRA, *Influence of injection mode on transport properties in kilometer-scale three-dimensional discrete fracture networks*, Water Resour. Res., 51 (2015), pp. 7289–7308.

[37] C. JENKINS, A. CHADWICK, AND S. D. HOVORKA, *The state of the art in monitoring and verification—Ten years on*, Int. J. Greenh. Gas. Con., 40 (2015), pp. 312–349.

[38] S. JOYCE, L. HARTLEY, D. APPLEGATE, J. HOEK, AND P. JACKSON, *Multi-scale groundwater flow modeling during temperate climate conditions for the safety assessment of the proposed high-level nuclear waste repository site at Forsmark, Sweden*, Hydrogeol. J., 22 (2014), pp. 1233–1249.

[39] P. KANG, S. BROWN, AND R. JUANES, *Emergence of anomalous transport in stressed rough fractures*, Earth Planet. Sci. Lett., 454 (2016), pp. 46–54.

[40] P. K. KANG, M. DENTZ, T. LE BORGNE, AND R. JUANES, *Anomalous transport on regular fracture networks: Impact of conductivity heterogeneity and mixing at fracture intersections*, Phys. Rev. E, 92 (2015), 022148.

[41] M. KARIMI-FARD AND L. J. DURLOFSKY, *A general gridding, discretization, and coarsening methodology for modeling flow in porous formations with discrete geological features*, Adv. Water Resour., 96 (2016), pp. 354–372.

[42] S. KARRA, N. MAKEDONSKA, H. VISWANATHAN, S. PAINTER, AND J. HYMAN, *Effect of advective flow in fractures and matrix diffusion on natural gas production*, Water Resour. Res., 51 (2015), pp. 8646–8657.

[43] S. KARRA, D. O'MALLEY, J. HYMAN, H. VISWANATHAN, AND G. SRINIVASAN, *Modeling flow and transport in fracture networks using graphs*, Phys. Rev. E, 97 (2018), 033304.

[44] A. Kreft and A. Zuber, *On the physical meaning of the dispersion equation and its solutions for different initial and boundary conditions*, Chem. Eng. Sci., 33 (1978), pp. 1471–1480.

[45] B. H. Kueper and D. B. McWhorter, *The behavior of dense, nonaqueous phase liquids in fractured clay and rock*, Ground Water, 29 (1991), pp. 716–728.

[46] P. Lichtner, G. Hammond, C. Lu, S. Karra, G. Bisht, B. Andre, R. Mills, and J. Kumar, *PFLOTRAN User Manual: A Massively Parallel Reactive Flow and Transport Model for Describing Surface and Subsurface Processes*, Tech. report LA-UR-15-20403, Los Alamos National Laboratory, Los Alamos, NM, 2015.

[47] J. Maillot, P. Davy, R. Le Goc, C. Darcel, and J.-R. De Dreuzy, *Connectivity, permeability, and channeling in randomly distributed and kinematically defined discrete fracture network models*, Water Rescour. Res., 52 (2016), pp. 8526–8545.

[48] N. Makedonska, J. D. Hyman, S. Karra, S. L. Painter, C. W. Gable, and H. S. Viswanathan, *Evaluating the effect of internal aperture variability on transport in kilometer scale discrete fracture networks*, Adv. Water Resour., 94 (2016), pp. 486–497.

[49] N. Makedonska, S. L. Painter, Q. M. Bui, C. W. Gable, and S. Karra, *Particle tracking approach for transport in three-dimensional discrete fracture networks*, Comput. Geosci., 19 (2015), pp. 1123–1137.

[50] P. Meakin and A. M. Tartakovsky, *Modeling and simulation of pore-scale multiphase fluid flow and reactive transport in fractured and porous media*, Rev. Geophys., 47 (2009), RG3002.

[51] K. Menger, *Zur allgemeinen kurventheorie*, Fund. Math., 10 (1927), pp. 96–115.

[52] R. Middleton, J. Carey, R. Currier, J. Hyman, Q. Kang, S. Karra, J. Jiménez-Martínez, M. Porter, and H. Viswanathan, *Shale gas and non-aqueous fracturing fluids: Opportunities and challenges for supercritical CO_2*, Appl. Energ., 147 (2015), pp. 500–509.

[53] National Research Council, *Rock Fractures and Fluid Flow: Contemporary Understanding and Applications*, National Academy Press, Washington, DC, 1996.

[54] S. Neuman, *Trends, prospects and challenges in quantifying flow and transport through fractured rocks*, Hydrogeol. J., 13 (2005), pp. 124–147.

[55] B. Noetinger and N. Jarrige, *A quasi steady state method for solving transient Darcy flow in complex 3D fractured networks*, J. Comput. Phys., 231 (2012), pp. 23–38.

[56] D. O'Malley, S. Karra, H. Hyman, J. D. Viswanathan, and G. Srinivasan, *Efficient Monte Carlo with graph-based subsurface flow and transport models*, Water Resour. Res., 54 (2018), pp. 3758–3766.

[57] S. L. Painter, C. W. Gable, and S. Kelkar, *Pathline tracing on fully unstructured control-volume grids*, Comput. Geosci., 16 (2012), pp. 1125–1134.

[58] Y.-J. Park, K.-K. Lee, G. Kosakowski, and B. Berkowitz, *Transport behavior in three-dimensional fracture intersections*, Water Resour. Res., 39 (2003), 1215, https://doi.org/10.1029/2002WR001801.

[59] G. Pichot, J. Erhel, and J.-R. de Dreuzy, *A mixed hybrid mortar method for solving flow in discrete fracture networks*, Appl. Anal., 89 (2010), pp. 1629–1643.

[60] G. Pichot, J. Erhel, and J.-R. de Dreuzy, *A generalized mixed hybrid mortar method for solving flow in stochastic discrete fracture networks*, SIAM J. Sci. Comput., 34 (2012), pp. B86–B105, https://doi.org/10.1137/100804383.

[61] A. Rasmuson and I. Neretnieks, *Radionuclide transport in fast channels in crystalline rock*, Water Resour. Res., 22 (1986), pp. 1247–1256.

[62] C. B. Rizzo and F. P. de Barros, *Minimum hydraulic resistance and least resistance path in heterogeneous porous media*, Water Rescour. Res., 53 (2017), pp. 8596–8613.

[63] H. Rubin and R. W. Buddemeier, *Transverse dispersion of contaminants in fractured permeable formations*, J. Hydrol., 176 (1996), pp. 133–151.

[64] P. N. Sævik and C. W. Nixon, *Inclusion of topological measurements into analytic estimates of effective permeability in fractured media*, Water Resour. Res., 53 (2017), pp. 9424–9443, https://doi.org/10.1002/2017WR020943.

[65] X. Sanchez-Vila, A. Guadagnini, and J. Carrera, *Representative hydraulic conductivities in saturated groundwater flow*, Rev. Geophys., 44 (2006), RG3002.

[66] E. Santiago, M. Romero-Salcedo, J. X. Velasco-Hernández, L. G. Velasquillo, and J. A. Hernández, *An integrated strategy for analyzing flow conductivity of fractures in a naturally fractured reservoir using a complex network metric*, in Advances in Computational Intelligence: 11th Mexican International Conference on Artificial Intelligence, MICAI 2012, San Luis Potosí, Mexico, 2012. Revised Selected Papers, Part II, I. Batyrshin and M. G. Mendoza, eds., Springer, Berlin, Heidelberg, 2013, pp. 350–361.

[67] E. Santiago, J. X. Velasco-Hernández, and M. Romero-Salcedo, *A methodology for the*

characterization of flow conductivity through the identification of communities in samples of fractured rocks, Expert Syst. Appl., 41 (2014), pp. 811–820.

[68] E. Santiago, J. X. Velasco-Hernández, and M. Romero-Salcedo, *A descriptive study of fracture networks in rocks using complex network metrics*, Comput. Geosci., 88 (2016), pp. 97–114.

[69] R. Sedgewick and K. Wayne, *Algorithms*, Addison-Wesley, Reading, MA, 2016.

[70] S. B. Seidman, *Network structure and minimum degree*, Soc. Networks, 5 (1983), pp. 269–287.

[71] D. Sidhu, R. Nair, and S. Abdallah, *Finding disjoint paths in networks*, in ACM SIGCOMM Computer Communication Review, 21, ACM, New York, 1991, pp. 43–51.

[72] G. Srinivasan and K. Lipnikov, *On the reconstruction of Darcy velocity in finite-volume methods*, Transport Porous Med., 96 (2013), pp. 337–351.

[73] J. Suurballe, *Disjoint paths in a network*, Networks, 4 (1974), pp. 125–145.

[74] J. W. Suurballe and R. E. Tarjan, *A quick method for finding shortest pairs of disjoint paths*, Networks, 14 (1984), pp. 325–336.

[75] A. R. Tyukhova and M. Willmann, *Connectivity metrics based on the path of smallest resistance*, Adv. Water Resour., 88 (2016), pp. 14–20.

[76] M. Valera, Z. Guo, P. Kelly, S. Matz, V. A. Cantu, A. G. Percus, J. D. Hyman, G. Srinivasan, and H. S. Viswanathan, *Machine learning for graph-based representations of three-dimensional discrete fracture networks*, Comput. Geosci., 22 (2018), pp. 695–710, https://doi.org/10.1007/s10596-018-9720-1.

[77] J. VanderKwaak and E. Sudicky, *Dissolution of non-aqueous-phase liquids and aqueous-phase contaminant transport in discretely-fractured porous media*, J. Contam. Hydrol., 23 (1996), pp. 45–68.

[78] T. P. Wellman, A. M. Shapiro, and M. C. Hill, *Effects of simplifying fracture network representation on inert chemical migration in fracture-controlled aquifers*, Water Resour. Res., 45 (2009), W01416.

[79] L. Zou, L. Jing, and V. Cvetkovic, *Modeling of flow and mixing in 3D rough-walled rock fracture intersections*, Adv. Water Resour., 107 (2017), pp. 1–9.